Studying the heterogeneity of the $Cr_xTi_{1-x}Ch_2$ (Ch = S, Se) single crystals using X-ray scanning photoemission microscopy

A.I.Merentsov[1], A.S.Shkvarin[1], M.S.Postnikov[1], L.Gregoratti[2], M.Amati[2], P.Zeller[2], P.Moras[3], A.N.Titov[1]

[1] M. N. Miheev Institute of Metal Physics of Ural Branch (UrD) of Russian Academy of Sciences (RAS), 620990 Ekaterinburg, Russia

[2] Elettra-Sincrotrone Trieste S.C.p.A., SS14-Km163.5 in Area Science Park, 34149 Trieste, Italy

[3] Istituto di Struttura della Materia-CNR (ISM-CNR), I-34149, Trieste, Italy

Abstract

The morphology of the heterogeneous $Cr_xTi_{1-x}Se_2$ and $Cr_xTi_{1-x}S_2$ single crystals has been studied using X-ray scanning photoemission microscopy (SPEM) and angular resolved photoemission spectroscopy (ARPES). A direct method of SPEM provided us the insight into the origin of the blurred ARPES images for $Cr_{0.78}Ti_{0.36}Se_2$ single crystal. Using SPEM, we confirmed the formation of the $CrSe_2$-based structural fragments inside the $Cr_xTi_{1-x}Se_2$ single crystals with $x \geq 0.75$. The chemical composition of the forming structural fragments depends on the chalcogen (S, Se) forming the crystal lattice.

Introduction

Layered transition metal dichalcogenides (LTMDs) and their intercalates attracted the scientific interest for decades [1–9]. Some of them are known for the strong electron-phonon interaction resulting in superconductivity [8,10–12] and/or charge-density-wave state [13–16]. Due to high ionic mobility, intercalation compounds based on LTMDs are used as electrolytes in Li-ion batteries [17–20]. Some direct-bandgap semiconductors like MoS_2 are suitable for application as photodetectors [21–23]. One of the promising areas of practical use of LTMDs is the spintronics [24–28]. Solid solutions of $Cr_xTi_{1-x}Ch_2$ (Ch = S, Se) are suitable for this purpose, as evidenced both by theoretical [29,30] and experimental [31–33] studies. Particularly, our previous study confirmed a 100% spin polarization in the $Cr_xTi_{1-x}Se_2$ at $x > 0.75$ [31]. To map the Fermi surface and electronic band structure of these materials, we need to measure the angle-resolved photoemission spectra (ARPES). This information is necessary to complete our knowledge about the spectrum of the charge carriers in these compounds. However, in literature there is no information about the electronic structure of Cr-substituted $TiCh_2$ (Ch = S, Se) compounds according to the ARPES studies. We assumed that the difficulties are concerned with the formation of heterogeneous structural fragments inside the $Cr_xTi_{1-x}Ch_2$ (Ch = S, Se) single crystals. This assumption originated from the X-ray photoelectron spectra (XPS) of the

$Cr_{0.83}Ti_{0.26}Se_2$ single crystal [31], where the contributions to the Se 3d spectrum from the Se atoms with different coordination by the Cr and Ti atoms were clearly seen.

The current study is aimed to prove the existence of the structural fragments inside the $Cr_xTi_{1-x}Ch_2$ (Ch = S, Se) single crystals as well as to study the chemical homogeneity of their surface.

Experiment

Polycrystalline samples of $Cr_xTi_{1-x}Se_2$ and $Cr_xTi_{1-x}S_2$ were synthesized by the high-temperature solid state reaction method in evacuated quartz ampoules [31,34]. X-ray powder diffraction showed a good quality of the samples. Single crystals in the shape of thin plates with the plane dimensions of about 2×2 mm^2 were grown from the polycrystalline phase using the gas transport technique with iodine as a gas-carrier [35]. The chemical composition of the single crystals was determined using energy dispersive X-ray analysis on a JEOL-733 spectrometer.

X-ray photoelectron spatially resolved XPS spectromicroscopy measurements were performed at the ESCA Microscopy beamline at the Elettra synchrotron facility (Trieste, Italy), with the hosted Scanning PhotoElectron Microscope (SPEM). SPEM measurements were carried out using photon energy of 651 eV. The photoelectrons were collected and analyzed with a SPECS-PHOIBOS Class 100 hemispherical analyzer equipped with a 48-channel electron detector. In the SPEM the X-ray beam is focused on the sample by a Fresnel Zone-Plate focusing optic and the chemical images are acquired by collecting core level photoelectrons emitted within the relevant kinetic energy window while raster scanning the specimen with respect to the microprobe [36]. The 48 channels electron detector allows to highlight in the image the lateral distribution of the different chemical states and to remove the topographic contributions. At each scanned position the corresponding 48 points XPS spectrum defined by the selected window energy is stored. By properly choosing the map acquisition energy and analyzing each of these spectra it is possible to create maps corresponding to specific spectra features distribution. All presented maps are showed and analyzed to represent only the pure chemical distribution of elements. For more information about the data analysis see ref [37].

The ARPES experiment was performed at the VUV photoemission beamline at Elettra synchrotron facility (Trieste, Italy). The single crystal samples were cleaved at room temperature in a vacuum chamber at a pressure better than 1×10^{-9} Torr. Spectra were acquired with a photon energy of E_{exc} = 45 eV, at a temperature of 9.6 K, using a Scienta R-4000 electron analyzer. The total energy and angular resolution were set to 15 meV and 0.3°, respectively. The LEED image

was obtained at the same beamline in the preparation chamber of the spectrometer at a pressure of $2 \cdot 10^{-10}$ mbar. The energy of the electrons was set to 100 eV.

Results

This assumption about the formation of the structural fragments with different metal-chalcogen chemical bonding within the single crystal became reasonable when we tried to obtain ARPES images from single-crystal samples of $Cr_{0.78}Ti_{0.36}Se_2$. Fig.1 shows typical ARPES images for these single crystals. Although the bands are visible, the image is blurred. This should be caused by the disordered structural fragments. However, since the band structure is still visible, either the angle between the fragments should be small or the fragments should be large enough.

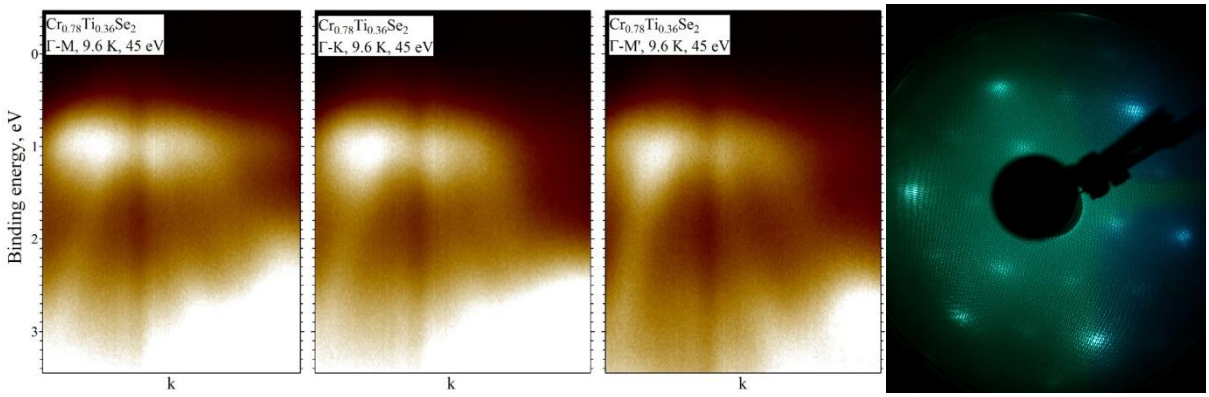

Figure 1. ARPES images obtained in Γ-M, Γ-K and Γ-M' directions for the $Cr_{0.78}Ti_{0.36}Se_2$ single crystal. On the right panel: LEED pattern demonstrates the duplication of the lattice parameters due to the superstructure formation.

Figure 2 shows the SPEM images of a 100×100 μm^2 surface of a $Cr_{0.78}Ti_{0.36}Se_2$ single crystal obtained at Se 3d, Ti 2p and Cr 3p. The cleaved surface was obtained in a vacuum chamber at a pressure of at least 1×10^{-9} Torr.

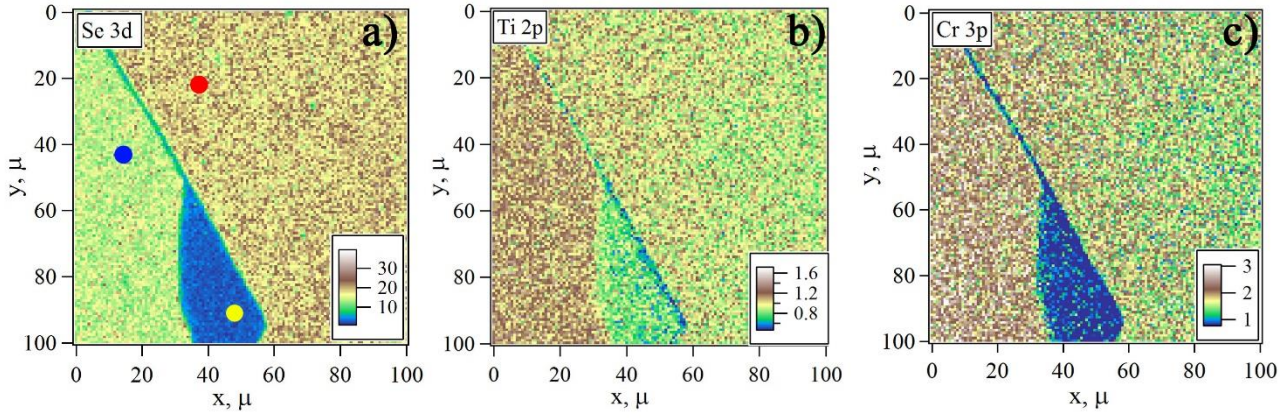

Figure 2. SPEM images of the $Cr_{0.78}Ti_{0.36}Se_2$ single crystal obtained at Se 3d (panel a), Ti 2p (panel b) and Cr 3p (panel c). Blue, red and yellow points in the left panel indicate the regions, where the survey spectra were obtained (see Fig. 3). The gradient scales show the intensity of the corresponding XPS peak.

There is a slight difference in the intensities of the Cr 3p (Fig.2c) and Ti 2p (Fig. 2b) lines for the areas marked with blue and red points. These are the average intensities ratios as calculated from the maps: $I_{red}/I_{blue}(Ti) \approx 0.87$, $I_{red}/I_{blue}(Cr) \approx 0.8$. The intensity of the Se 3d line changes more significantly: $I_{red}/I_{blue}(Se) \approx 1.3$.

Figure 3 shows the survey spectra for the regions marked with red, blue and yellow points. One can see a good quality of the surface marked with red and blue points according to the absence of the O 1s peak and relatively low intensity of the C 1s peak. Moreover, the survey spectra for these points are almost identical. In its turn, the area marked with the yellow point corresponds to the uncleaved surface of the single crystal.

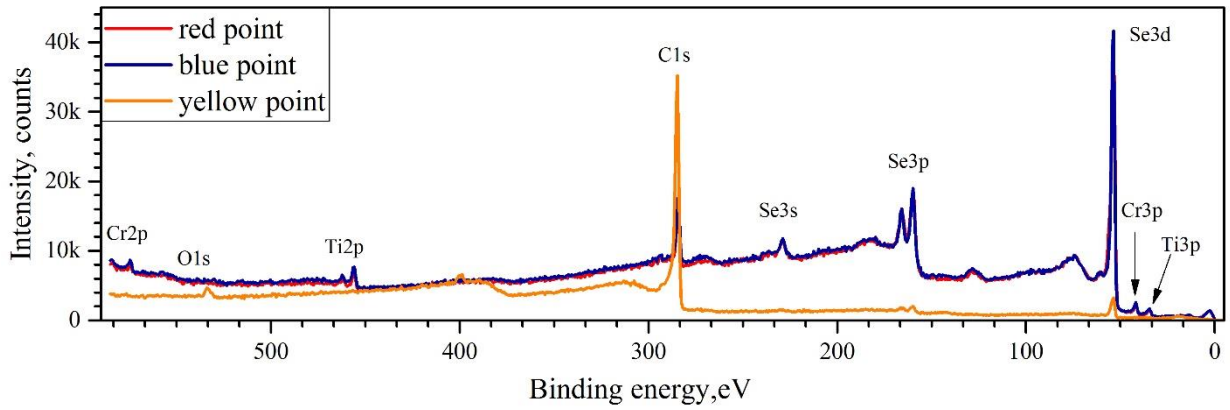

Figure 3. Survey spectra for $Cr_{0.78}Ti_{0.36}Se_2$ collected in red, blue and yellow points (see Fig. 2).

For a more thorough study of the surface of the $Cr_{0.78}Ti_{0.36}Se_2$ single crystal, the detailed core level spectra of the main detected elements were obtained for the areas marked with red and blue points. Fig. 4 shows the Cr 3p (together with Ti 3p), Ti 2p and Cr $2p_{3/2}$ core level spectra. One can see that the I(Cr 3p)/I(Ti 3p) intensity ratio does not change moving from the red to the blue points (Fig. 4, left panel). It should be noted that the spectra shown in Figure 4 are normalized to the maximum intensity. The Ti 2p spectra are almost identical to those obtained previously for the $Cr_xTi_{1-x}Se_2$ system [38]. The energy position of the Cr $2p_{3/2}$ line is the same as reported previously for these compounds [31,38], however the intensities of the Cr $2p_{3/2}$ subpeaks (with E_B = 573.7 eV and E_B = 574.7 eV) slightly differs. This difference can be attributed to the limited signal to noise ratio in the current study which makes difficult a precise assignment of the energy peak position. Nevertheless, the typical 1 eV-splitting of the Cr $2p_{3/2}$ line due to the spin polarization of the Cr electrons [31] is well visible for both regions.

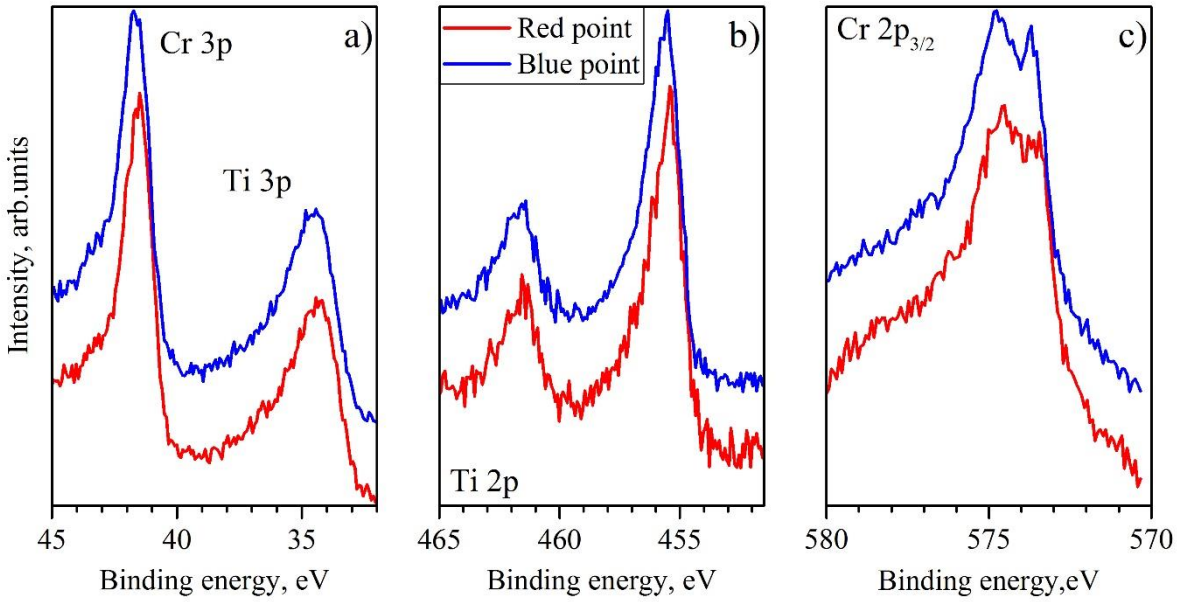

Figure 4. Ti 3p, Cr 3p (panel a), Ti 2p (panel b) and Cr $2p_{3/2}$ (panel c) core level spectra for $Cr_{0.78}Ti_{0.36}Se_2$ collected in the red and the blue points (see Fig. 2).

As mentioned above, the major visible difference for the regions marked with the red and the blue points appears in the Se 3d contrast (Fig. 2, left panel). Fig. 5, central panel, shows the averaged Se 3d spectra from the areas marked as colored rectangles as extracted from the 48 channels maps. Unfortunately, we are not able to present the Se 3d spectra collected specific points as we have done for Cr 3p, Cr 2p and Ti 2p spectra, due to the radiation induced degradation of the upper layer of the crystals, which is the Se layer in the studied compounds, during a long time exposure as needed for the detailed core level spectra acquisition. Such detrimental effect is avoided in the acquisition of chemical maps because of the short exposure time per pixel which is of the order of a few tens of ms compared to the minutes needed for core level spectrum acquisition. Despite the energy resolution used for mapping is slightly poorer than that set for the acquisition of spectra the 48 points extracted from maps are highly informative. As a matter of comparison, the Se 3d detailed core level spectrum from $TiSe_2$ is reported in the panel; due to the higher energy resolution condition the spin-orbit splitting is better resolved if compared, for instance, to the spectrum of the red area. One can clearly see that the spectra collected from the blue and brown areas contain an additional shoulder (marked as energy region II) compared to the spectra collected from the red and green areas (marked as energy region I): a similar behavior was previously observed on $Cr_{0.83}Ti_{0.26}Se_2$ [31]. The Se 3d spectrum for $Cr_{0.83}Ti_{0.26}Se_2$ is shown in Fig. 5 (central panel) for comparison as well. States in region I correspond to Se in $TiSe_2$ while those of region II correspond to Se in $CrSe_2$. The spatial distribution of the spectral intensities defined as energy region I and region II in Fig.5 central

panel is shown in the right panel where the ratio of the maps calculated on each energy regions has been calculated. It is clearly seen that there are different Se states in the structural fragments.

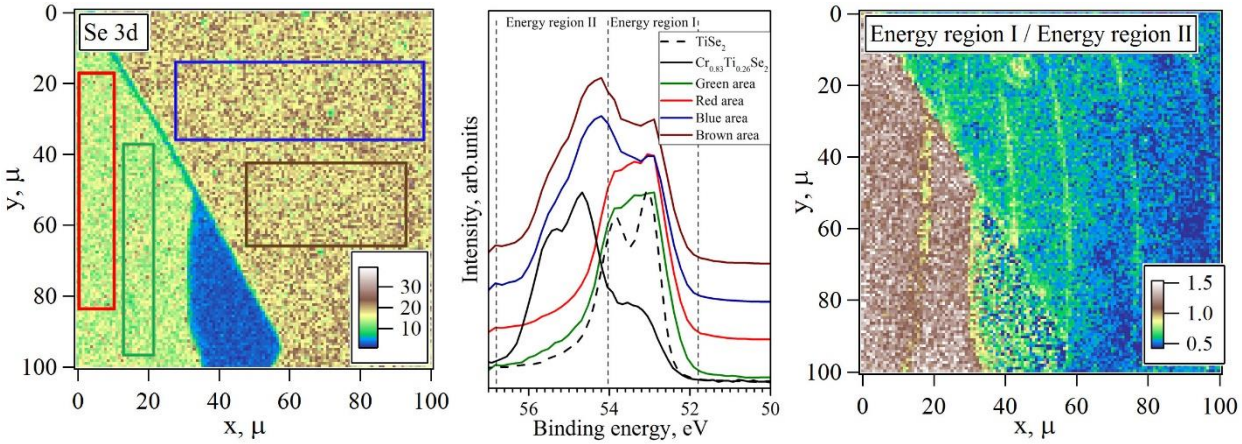

Figure 5. Left panel: SPEM image for the $Cr_{0.78}Ti_{0.36}Se_2$ single crystal obtained at Se 3d. The gradient scale shows the value of the elemental intensity ratio. Central panel: Se 3d core level spectra for $Cr_{0.78}Ti_{0.36}Se_2$ collected from areas marked as colored rectangles on the left panel along with Se 3d spectra for previously investigated $Cr_{0.83}Ti_{0.26}Se_2$ (black line) and $TiSe_2$ (dashed line) [31]; energy regions I and II correspond to the different Se $3d_{5/2}$ states. Right panel: map in the Se 3d contrast plotted as I_I/I_{II} intensity ratio in each point, where I_I and I_{II} are the intensities of the Se $3d_{5/2}$ peak in regions I and II (left panel), respectively. The gradient scale shows the value of the I_I/I_{II} intensity ratio.

Fig. 6 shows the SPEM images of a 100×100 μm^2 surface of the $Cr_{0.34}Ti_{0.66}S_2$ single crystal obtained at S 2p core levels, and Cr 3p/Ti 3p ratio.

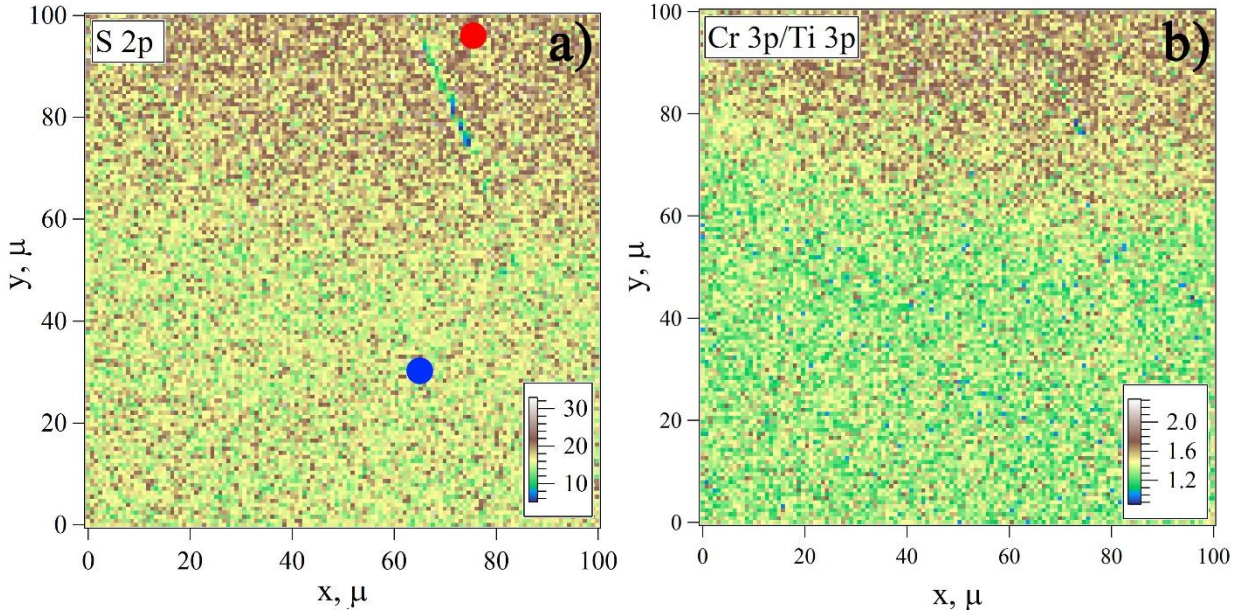

Figure 6. SPEM images of the $Cr_{0.34}Ti_{0.66}S_2$ single crystal obtained at S 2p (panel a) and Cr 3p/Ti 3p ratio (panel b). The blue and the red points in the left panel indicate the regions, where the survey spectra were obtained (see Fig. 7). The gradient scales show the value of the elemental intensity ratio.

In the sulfur SPEM image a contrast between two phases is visible, but the differences are very low, and the S distribution can be assumed to be almost uniform compared to the other elements. Fig. 7 shows the survey spectra collected in “blue-point” and “red-point” regions for $Cr_{0.34}Ti_{0.36}S_2$. The only visible difference in these survey spectra is in the relative intensity of the C 1s peak. There is no visible difference for other XPS peaks in the survey spectra. For a more thorough study of the surface of the $Cr_{0.34}Ti_{0.66}S_2$ single crystal, the core level spectra of the main detected elements were collected in the areas marked with the red and the blue points (Fig. 8). All the core level spectra are normalized to the maximum intensity. It is clearly seen the decrease of the intensity of the Cr 3p line with respect to the intensity of the Ti 3p line while moving from the “red-point” to “blue-point” region. This corresponds to the decrease of the relative amount of Cr content in the “blue-point” region with respect to the “red-point” region. This is in line with the Cr 3p/Ti 3p ratio obtained from the corresponding SPEM maps shown in Fig. 6-b). Considering the photoionization cross-sections for Cr 3p and Ti 3p lines [39] one can estimate the Cr / Ti ratio in the “red-point” and “blue-point” regions. For the “red-point” region, if we take the sum of metals as 1, the ratio corresponds to $Cr_{0.39}Ti_{0.61}$, for the “blue” region to $Cr_{0.2}Ti_{0.8}$.

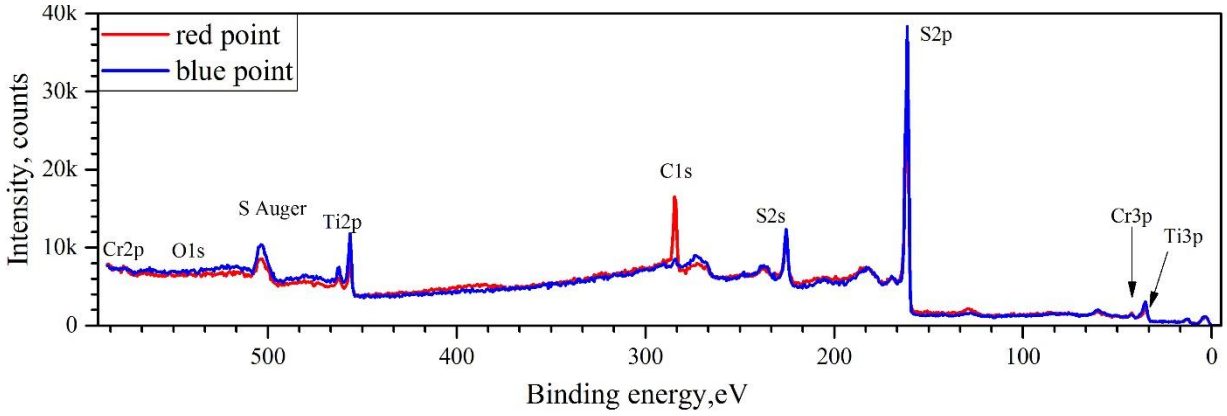

Figure 7. Survey spectra for $Cr_{0.34}Ti_{0.66}S_2$ collected in the red and the blue points (see Fig. 6).

The Ti 2p line gradually shifts toward the low binding energy as the Cr concentration in the fragment increases. For the “blue-point” region the energy shift equals to 0.23 eV as compared to Ti 2p line for TiS_2; for the “red-point” region this shift equals to 0.43 eV. Cr 2p spectra differ in “red-point” and “blue-point” regions. The typical 1eV splitting is visible on the Cr 2p spectra collected both from the “blue-point” (a region with lower Cr content) and “red-point” (a region with higher Cr content) regions. We have shown previously that the splitting of Cr $2p_{3/2}$ line disappears at reaching the percolation threshold in the Cr sublattice [40]. In fact, the Cr $2p_{3/2}$ splitting is better visible for the “blue-point” region than for the “red-point” one, which is in a

good agreement with our previous results for the Cr_xTiSe_2 system [40]. The S 2p core level spectrum does not change and coincide with that for TiS_2.

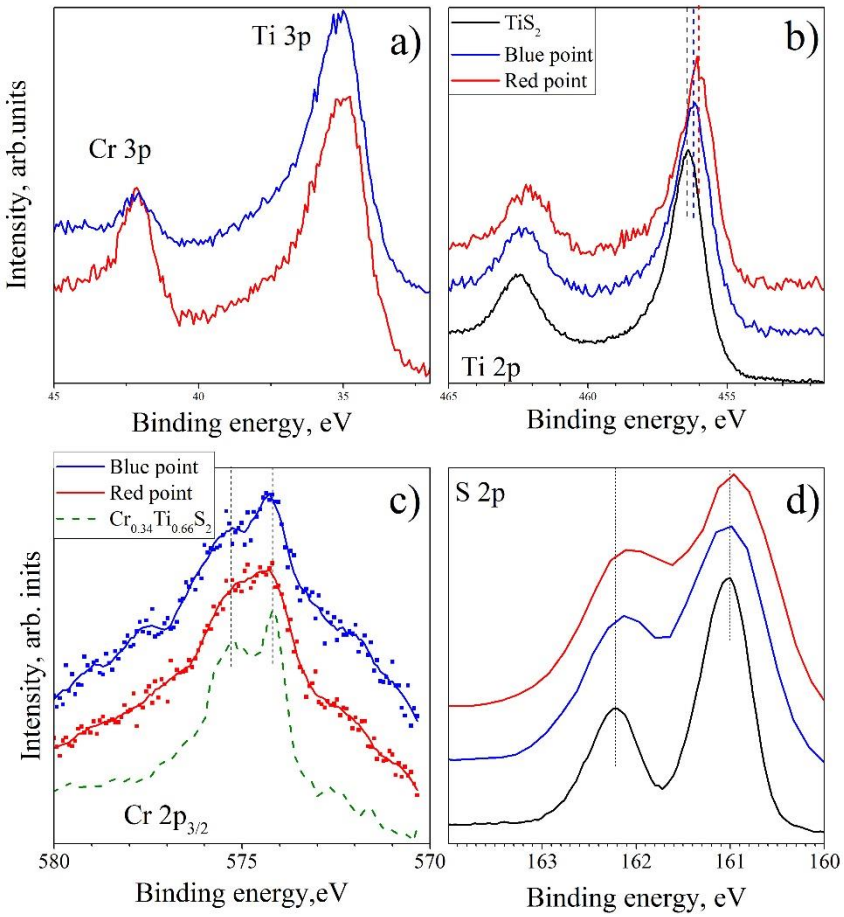

Figure 8. Ti 3p, Cr 3p (panel a), Ti 2p (panel b), Cr $2p_{3/2}$ (panel c) and S 2p (panel d) core level spectra for $Cr_{0.34}Ti_{0.66}S_2$ collected in the red and the blue points (see Fig. 7). The dashed lines in the b) and c) panels mark up the energy position of the Ti $2p_{3/2}$ line (panel b) and Cr $2p_{3/2}$ components (panel c). On the panel c) the solid line shows the smoothing of the experimental spectrum shown by dots.

Discussion

The SPEM experimental results clearly indicate the presence of structural domain in the single crystals of $Cr_xTi_{1-x}Ch_2$ (Ch = S, Se). These fragments differ in the chemical composition and chemical bonding. Because the single crystals grow from the gas phase, the equilibrium is reached very quickly, and the formation of such fragments cannot be the result of the decomposition of a solid solution but must occur during the crystallization process. In $Cr_{0.78}Ti_{0.36}Se_2$, the fragments consist of a $TiSe_2$-based solid solution ($Cr_xTi_{1-x}Se_2$, corresponds to the energy region I in Fig. 5) and a $CrSe_2$-based solid solution ($Ti_xCr_{1-x}Se_2$, corresponds to the energy region II in Fig. 5). The structural fragments are slightly disordered, which follows from the mismatch of the growth step in two fragments (the growth steps are visible as stripes in Fig.

5, right panel). The growth steps on right panel of figure 5 are shifted by about 4 μm. The blurring of the ARPES image for this crystal may be caused by the falling of the incident beam onto several fragments of different types.

In $Cr_{0.34}Ti_{0.66}S_2$, the formation of the structural fragments of various chemical compositions is also observed. However, there is no significant change in the chemical bonding between S and environment in different fragments. This indicates the formation of the $Cr_xTi_{1-x+y}S_2$ fragments differing in the content of superstoichiometric Ti(y). Unfortunately, we cannot obtain the information about the degree of disordering of structural fragments based on the SPEM image. The difference in chemical composition should increase the Fermi energy in fragments with a large excess of Ti. This should result in the gradual energy shift of both Cr and Ti XPS spectra in the same direction. However, only the binding energy of Ti2p line slightly changes. This indicates that the concentration of electrons is nearly the same in all structural fragments, i.e. the Fermi energy does not change from fragment to fragment. Therefore, we can conclude that the structural fragments are in close, possibly coherent, relation, and fragments with high concentration of excess Ti donate electrons stabilizing the $Cr_xTi_{1-x}S_2$ solid solution.

In $Cr_{0.78}Ti_{0.36}Se_2$, there is a slight difference in the binding energies of Ti 2p, 3p and Cr 2p, 3p lines for red and blue point areas. For the blue point area ($TiSe_2$-based solid solution $Cr_xTi_{1-x}Se_2$) the binding energies are slightly higher than those for the red point area ($CrSe_2$-based solid solution $Ti_xCr_{1-x}Se_2$). Firstly, this means that red point area donates electrons. Secondly, either the electric contact between these structural fragments can be much worse than that in $Cr_{0.34}Ti_{0.66}S_2$ or the size of the fragments is much larger, bringing the material to the mixture of phases.

Conclusion

The formation of the $TiSe_2$-based and $CrSe_2$-based structural fragments in the $Cr_{0.78}Ti_{0.36}Se_2$ single crystal was confirmed experimentally using SPEM technique. This morphology may be responsible for the blurring of the preliminary obtained ARPES images of this crystal. The fragments are also formed in $Cr_{0.34}Ti_{0.66}S_2$, however they differ not in the chemical bonding of chalcogen, like in $Cr_{0.78}Ti_{0.36}Se_2$, but in the concentration of superstoichiometric Ti. The results obtained allow to conclude the stability of the $CrSe_2$-based fragments inside the $Cr_xTi_{1-x}Se_2$ single crystals. This information is useful for further study of the $CrSe_2$-based materials and their application in spintronics.

Acknowledgments

The research was carried out within the state assignment of the Ministry of Education and Science of Russia (theme “Spin” No. AAAA-A18-118020290104-2 and theme “Electron” No. AAAA-A18-118020190098-5). The reported study was funded by RFBR, project number 19-33-60031.This project has received funding from the EU-H2020 research and innovation program under grant agreement No 654360 having benefitted from the Access provided by IOM-CNR in Trieste (Italy) within the framework of the NFFA-Europe Transnational Access Activity.

Data Availability

The data that support the findings of this study are available from the corresponding author upon reasonable request.

Bibliography

[1] J.A. Wilson, A.D. Yoffe, The transition metal dichalcogenides discussion and interpretation of the observed optical, electrical and structural properties, Adv. Phys. 18 (1969) 193–335. https://doi.org/10.1080/00018736900101307.

[2] D.W. Bullett, Electronic band structure and bonding in transition metal layered dichalcogenides by atomic orbital methods, J. Phys. C Solid State Phys. 11 (1978) 4501–4514. https://doi.org/10.1088/0022-3719/11/22/007.

[3] G.V.S. Rao, M.W. Shafer, Intercalation in Layered Transition Metal Dichalcogenides, in: Intercalated Layer. Mater., Springer Netherlands, Dordrecht, 1979: pp. 99–199. https://doi.org/10.1007/978-94-009-9415-7_3.

[4] R.B. Somoano, J.A. Woollam, Intercalated Layered Materials, Springer Netherlands, Dordrecht, 1979. https://doi.org/10.1007/978-94-009-9415-7.

[5] T. HIBMA, Structural Aspects of Monovalent Cation Intercalates of Layered Dichalcogenides, in: M.S.Wittingham and A.J.Jacobsen (Ed.), Intercalation Chem., Elsevier, 1982: pp. 285–313. https://doi.org/10.1016/b978-0-12-747380-2.50014-6.

[6] Q.H. Wang, K. Kalantar-Zadeh, A. Kis, J.N. Coleman, M.S. Strano, Electronics and optoelectronics of two-dimensional transition metal dichalcogenides, Nat. Nanotechnol. 7 (2012) 699–712. https://doi.org/10.1038/nnano.2012.193.

[7] M. Chhowalla, H.S. Shin, G. Eda, L.-J. Li, K.P. Loh, H. Zhang, The chemistry of two-dimensional layered transition metal dichalcogenide nanosheets, Nat. Chem. 5 (2013) 263–275. https://doi.org/10.1038/nchem.1589.

[8] Y.-T. Hsu, A. Vaezi, M.H. Fischer, E.-A. Kim, Topological superconductivity in monolayer transition

metal dichalcogenides, Nat. Commun. 8 (2017) 14985. https://doi.org/10.1038/ncomms14985.

[9] Y. Ominato, J. Fujimoto, M. Matsuo, Valley-Dependent Spin Transport in Monolayer Transition-Metal Dichalcogenides, Phys. Rev. Lett. 124 (2020) 166803. https://doi.org/10.1103/PhysRevLett.124.166803.

[10] E. Morosan, H.W. Zandbergen, B.S. Dennis, J.W.G. Bos, Y. Onose, T. Klimczuk, A.P. Ramirez, N.P. Ong, R.J. Cava, Superconductivity in Cu_xTiSe_2, Nat. Phys. 2 (2006) 544–550. https://doi.org/10.1038/nphys360.

[11] B.P. Clayman, R.F. Frindt, The superconducting energy gap of $NbSe_2$, Solid State Commun. 9 (1971) 1881–1884. https://doi.org/10.1016/0038-1098(71)90574-6.

[12] R.B. Somoano, A. Rembaum, Superconductivity in Intercalated Molybdenum Disulfide, Phys. Rev. Lett. 27 (1971) 402–404. https://doi.org/10.1103/PhysRevLett.27.402.

[13] M.M. Ugeda, A.J. Bradley, Y. Zhang, S. Onishi, Y. Chen, W. Ruan, C. Ojeda-Aristizabal, H. Ryu, M.T. Edmonds, H.-Z. Tsai, A. Riss, S.-K. Mo, D. Lee, A. Zettl, Z. Hussain, Z.-X. Shen, M.F. Crommie, Characterization of collective ground states in single-layer $NbSe_2$, Nat. Phys. 12 (2016) 92–97. https://doi.org/10.1038/nphys3527.

[14] J.Á. Silva-Guillén, P. Ordejón, F. Guinea, E. Canadell, Electronic structure of 2H-$NbSe_2$ single-layers in the CDW state, 2D Mater. 3 (2016) 035028. https://doi.org/10.1088/2053-1583/3/3/035028.

[15] D. Qian, D. Hsieh, L. Wray, Y. Xia, R.J. Cava, E. Morosan, M.Z. Hasan, Evolution of low-lying states in a doped CDW superconductor Cu_xTiSe_2, Phys. B Condens. Matter. 403 (2008) 1002–1004. https://doi.org/10.1016/j.physb.2007.10.240.

[16] Y. Miyahara, H. Bando, H. Ozaki, Tunnelling spectroscopy investigation of the CDW state in $TiSe_{2-x}S_x$, J. Phys. Condens. Matter. 8 (1996) 7453–7461. https://doi.org/10.1088/0953-8984/8/40/010.

[17] M.S. Whittingham, F.R. Gamble, The lithium intercalates of the transition metal dichalcogenides, Mater. Res. Bull. 10 (1975) 363–371. https://doi.org/10.1016/0025-5408(75)90006-9.

[18] C.M. Julien, Lithium intercalated compounds: Charge transfer and related properties, Mater. Sci. Eng. R Reports. 40 (2003) 47–102. https://doi.org/10.1016/S0927-796X(02)00104-3.

[19] C. Peng, H. Lyu, L. Wu, T. Xiong, F. Xiong, Z. Liu, Q. An, L. Mai, Lithium- and Magnesium-Storage Mechanisms of Novel Hexagonal $NbSe_2$, ACS Appl. Mater. Interfaces. 10 (2018) 36988–36995. https://doi.org/10.1021/acsami.8b12662.

[20] P. Li, X. Zheng, H. Yu, G. Zhao, J. Shu, X. Xu, W. Sun, S.X. Dou, Electrochemical potassium/lithium-ion intercalation into $TiSe_2$: Kinetics and mechanism, Energy Storage Mater. 16 (2019) 512–518.

https://doi.org/10.1016/j.ensm.2018.09.014.

[21] K. Zhang, X. Fang, Y. Wang, Y. Wan, Q. Song, W. Zhai, Y. Li, G. Ran, Y. Ye, L. Dai, Ultrasensitive Near-Infrared Photodetectors Based on a Graphene–$MoTe_2$–Graphene Vertical van der Waals Heterostructure, ACS Appl. Mater. Interfaces. 9 (2017) 5392–5398. https://doi.org/10.1021/acsami.6b14483.

[22] O. Lopez-Sanchez, D. Lembke, M. Kayci, A. Radenovic, A. Kis, Ultrasensitive photodetectors based on monolayer MoS_2, Nat. Nanotechnol. 8 (2013) 497–501. https://doi.org/10.1038/nnano.2013.100.

[23] K. Roy, M. Padmanabhan, S. Goswami, T.P. Sai, G. Ramalingam, S. Raghavan, A. Ghosh, Graphene–MoS_2 hybrid structures for multifunctional photoresponsive memory devices, Nat. Nanotechnol. 8 (2013) 826–830. https://doi.org/10.1038/nnano.2013.206.

[24] C.F. van Bruggen, R.J. Haange, G.A. Wiegers, D.K.G. de Boer, $CrSe_2$, a new layered dichalcogenide, Phys. B+C. 99 (1980) 166–172. https://doi.org/10.1016/0378-4363(80)90226-0.

[25] N. Sirica, S.K. Mo, F. Bondino, I. Pis, S. Nappini, P. Vilmercati, J. Yi, Z. Gai, P.C. Snijders, P.K. Das, I. Vobornik, N. Ghimire, M.R. Koehler, L. Li, D. Sapkota, D.S. Parker, D.G. Mandrus, N. Mannella, Electronic structure of the chiral helimagnet and 3d -intercalated transition metal dichalcogenide $Cr_{1/3}NbS_2$, Phys. Rev. B. 94 (2016) 075141. https://doi.org/10.1103/PhysRevB.94.075141.

[26] C. Huang, Y. Jin, W. Wang, L. Tang, C. Song, F. Xiu, Manganese and chromium doping in atomically thin MoS_2, J. Semicond. 38 (2017) 033004. https://doi.org/10.1088/1674-4926/38/3/033004.

[27] S. Manzeli, D. Ovchinnikov, D. Pasquier, O. V. Yazyev, A. Kis, 2D transition metal dichalcogenides, Nat. Rev. Mater. 2 (2017) 17033. https://doi.org/10.1038/natrevmats.2017.33.

[28] X. Zhao, T. Wang, C. Xia, X. Dai, S. Wei, L. Yang, Magnetic doping in two-dimensional transition-metal dichalcogenide zirconium diselenide, J. Alloys Compd. 698 (2017) 611–616. https://doi.org/10.1016/j.jallcom.2016.12.260.

[29] C.M. Fang, C.F. Van Bruggen, R.A. De Groot, G.A. Wiegers, C. Haas, The electronic structure of the metastable layer compound 1T-$CrSe_2$, J. Phys. Condens. Matter. 9 (1997) 10173–10184. https://doi.org/10.1088/0953-8984/9/46/015.

[30] T. Teshima, N. Suzuki, K. Motizuki, Electronic Band Structures of 1T-Type TiS_2 Intercalated with Light 3d Transition-Metals, J. Phys. Soc. Japan. 60 (1991) 1005–1010. https://doi.org/10.1143/JPSJ.60.1005.

[31] A.I. Merentsov, Y.M. Yarmoshenko, A.N. Skorikov, A.N. Titov, A. Buling, M. Räkers, M. Neumann,

E.G. Galieva, P.A. Slepuhin, Electronic structure of $Cr_xTi_{1-x}X_2$, X = S, Se solid solutions, J. Electron Spectros. Relat. Phenomena. 182 (2010) 70–75. https://doi.org/10.1016/j.elspec.2010.07.005.

[32] A.S. Shkvarin, M. V. Yablonkikh, Y.M. Yarmoshenko, A.I. Merentsov, B. V. Senkovskiy, J. Avila, M. Asensio, A.N. Titov, Electronic structure of octahedrally coordinated Cr in Cr_xTiX_2 (X = Se, Te) and $Ti_xCr_{1-x}Se_2$, J. Electron Spectros. Relat. Phenomena. 206 (2016) 12–17. https://doi.org/10.1016/j.elspec.2015.11.001.

[33] A.N. Titov, A. V. Kuranov, V.G. Pleschev, Y.M. Yarmoshenko, M. V. Yablonskikh, A. V. Postnikov, S. Plogmann, M. Neumann, A. V. Ezhov, E.Z. Kurmaev, Electronic structure of Co_xTiSe_2 and Cr_xTiSe_2, Phys. Rev. B - Condens. Matter Mater. Phys. 63 (2001) 035106. https://doi.org/10.1103/PhysRevB.63.035106.

[34] A.N. Titov, A.I. Merentsov, V.N. Neverov, Structure and properties of $Ti_{1-x}Cr_xSe_2$ substitutional solid solutions, Phys. Solid State. 48 (2006) 1472–1476. https://doi.org/10.1134/S1063783406080087.

[35] H.P.B. Rimmington, A.A. Balchin, B.K. Tanner, Nearly perfect single crystals of layer compounds grown by iodine vapour-transport techniques, J. Cryst. Growth. 15 (1972) 51–56. https://doi.org/10.1016/0022-0248(72)90319-3.

[36] P. Zeller, M. Amati, H. Sezen, M. Scardamaglia, C. Struzzi, C. Bittencourt, G. Lantz, M. Hajlaoui, E. Papalazarou, M. Marino, M. Fanetti, S. Ambrosini, S. Rubini, L. Gregoratti, Scanning Photoelectron Spectro-Microscopy: A Modern Tool for the Study of Materials at the Nanoscale, Phys. Status Solidi. 215 (2018) 1800308. https://doi.org/10.1002/pssa.201800308.

[37] L. Gregoratti, A. Barinov, E. Benfatto, G. Cautero, C. Fava, P. Lacovig, D. Lonza, M. Kiskinova, R. Tommasini, S. Mähl, W. Heichler, 48-Channel electron detector for photoemission spectroscopy and microscopy, Rev. Sci. Instrum. 75 (2004) 64–68. https://doi.org/10.1063/1.1630837.

[38] A.S. Shkvarin, Y.M. Yarmoshenko, N.A. Skorikov, A.I. Merentsov, A.N. Titov, P.A. Slepukhin, D.E. Marchenko, M. Sperling, Studying the electronic structure of $Cr_xTi_{1-x}Se_2$ by X-ray resonance and absorption spectroscopy, J. Exp. Theor. Phys. 112 (2011) 87–93. https://doi.org/10.1134/S1063776110061172.

[39] J.J. Yeh, I. Lindau, Atomic subshell photoionization cross sections and asymmetry parameters: $1 \leq Z \leq 103$, At. Data Nucl. Data Tables. 32 (1985) 1–155. https://doi.org/10.1016/0092-640X(85)90016-6.

[40] A.N. Titov, Y.M. Yarmoshenko, M. Neumann, V.G. Pleshchev, S.G. Titova, Hierarchy of percolation thresholds and the mechanism for reduction of magnetic moments of transition metals

intercalated into $TiSe_2$, Phys. Solid State. 46 (2004) 1681–1685. https://doi.org/10.1134/1.1799187.